Materials Today Physics 68 (2026) 102297

Contents lists available at ScienceDirect

Materials Today Physics

journal homepage: www.journals.elsevier.com/materials-today-physics

Bending-induced pseudo-piezoelectricity in suspended $FeTe_x$ nanosheets

Jing Chen [a,b,1], Jiefeng Ye [a,b,1], Yifei Ma [a,b], Changlin Chen [a,b], Shangrun Lu [c], Liwei Guan [a,b,*], Weijian Zhang [a,b], Hongyi Lu [a,b], Zhongchong Lin [a,b,**], Huaixi Chen [d,***], Guoyang Su [a,b], Yuling Zhou [a,b], Luis A. Montero-Cabrera [e,f], Oleg V. Kolosov [g], Licong Peng [c], Liqiang Zeng [a], Ziyang Gan [h,****], Zixuan Cao [a], Jianmin Zhang [a,b,*****], Yue Chen [a,b,******], Zhigao Huang [a,b]

[a] College of Physics and Energy, Fujian Normal University, Fujian Provincial Key Laboratory of Quantum Manipulation and New Energy Materials, Fuzhou, 350117, China
[b] Fujian Provincial Engineering Technical Research Centre of Solar-Energy Conversion and Stored Energy, Fuzhou, 350117, China
[c] School of Materials Science and Engineering, Peking University, Beijing, 100871, China
[d] College of Photonic Electronic Engineering, Fujian Normal University, Fuzhou, 350117, China
[e] Laboratorio de Química Computacional y Teórica, Departamento de Química Física, Universidad de La Habana, 10400, Havana, Cuba
[f] Donostia International Physics Center (DIPC), Donostia – San Sebastián, Basque Country, 20018, Spain
[g] Department of Physics, Lancaster University, Lancaster, LA1 4YB, UK
[h] School of Physics and Electronics, Hunan Normal University, Changsha, 410081, China

ARTICLE INFO

Keywords:
2D materials
Strain-gate transistor
CVD
Flexoelectricity
Interlayer sliding

ABSTRACT

The bending deformation-induced flexoelectricity, with its unique size dependence and lack of symmetry constraints, holds promise for two-dimensional van der Waals electronics. However, realizing this potential is fundamentally challenged by interlayer sliding during mechanical deformation—a ubiquitous yet less understood phenomenon that critically modulates flexoelectric and ferroelectric responses. In this work, we select CVD-grown layered FeTe and nonlayered $FeTe_2$ nanosheets as model systems to investigate how interlayer sliding affects the flexoelectricity. Combining Raman spectroscopy, nanoindentation, and strain-dependent piezoresponse force microscopy (PFM), we show that nonlayered $FeTe_2$ exhibits a linear flexoelectric response proportional to the strain gradient, whereas layered FeTe displays an anomalous nonlinearity in its pseudo-piezoelectric intensity. This anomalous behavior is accompanied by a thickness-dependent Young's modulus in FeTe and is attributed to interlayer sliding during deformation, as confirmed by neural network molecular dynamics simulations (NNMD) and first-principles calculations. Our results identify interlayer sliding as an important factor governing flexoelectricity in layered materials and suggest its potential as a tunable degree of freedom for engineering polarization in 2D devices.

* Corresponding author. College of Physics and Energy, Fujian Normal University, Fujian Provincial Key Laboratory of Quantum Manipulation and New Energy Materials, Fuzhou, 350117, China
** Corresponding author. College of Physics and Energy, Fujian Normal University, Fujian Provincial Key Laboratory of Quantum Manipulation and New Energy Materials, Fuzhou, 350117, China
*** Corresponding author.College of Photonic Electronic Engineering, Fujian Normal University, Fuzhou 350117, China
**** Corresponding author.School of Physics and Electronics, Hunan Normal University, Changsha 410081, China
***** Corresponding author. College of Physics and Energy, Fujian Normal University, Fujian Provincial Key Laboratory of Quantum Manipulation and New Energy Materials, Fuzhou, 350117, China
****** Corresponding author. College of Physics and Energy, Fujian Normal University, Fujian Provincial Key Laboratory of Quantum Manipulation and New Energy Materials, Fuzhou, 350117, China
E-mail addresses: zclin@fjnu.edu.cn (Z. Lin), chenhx@fjnu.edu.cn (H. Chen), ziyang@hunnu.edu.cn (Z. Gan), jmzhang@fjnu.edu.cn (J. Zhang), yuechen@fjnu.edu.cn (Y. Chen).
[1] J. C. and J. F. contribute equally.

https://doi.org/10.1016/j.mtphys.2026.102297
Received 27 August 2026; Received in revised form 27 October 2026; Accepted 27 October 2026
Available online 29 October 2026
2542-5293/© 2026 Elsevier Ltd. All rights are reserved, including those for text and data mining, AI training, and similar technologies.

1. Introduction

The flexoelectric effect [1] is an electromechanical coupling phenomenon in which non-uniform strain breaks inversion symmetry in a crystal, inducing electric polarization. This effect is universal across all material classes, as the polarization P_i is generated by strain gradients ($\frac{\partial \varepsilon_{jk}}{\partial x_l}$) according to $P_i = \mu_{ijkl}\frac{\partial \varepsilon_{jk}}{\partial x_l}$ [2]. Unlike piezoelectricity [3,4], which requires non-centrosymmetric crystals, flexoelectricity arises solely from gradient-induced symmetry breaking, making it possible to universally break inversion symmetry in any material. Recent studies have revealed that ice can generate flexoelectricity (and even ferroelectricity) [5], underscoring both the universality and the broad prospects of flexoelectricity. These characteristics enable phenomena typically exclusive to non-centrosymmetric materials—such as piezoelectricity [6–9]—to be induced in centrosymmetric systems.

The flexural deformation-induced flexoelectric effect is of critical significance in two-dimensional (2D) van der Waals materials [10,11]. Their atomic thinness and exceptional mechanical flexibility enable the generation of enormous strain gradients during bending, which in turn induce a strong flexoelectric polarization proportional to the strain gradient magnitude. This effect unlocks novel 2D device concepts, such as strain-programmable electronics, non-volatile memory, and micro-scale energy harvesters, that are unattainable with traditional bulk materials [8,9,12]. However, a fundamental challenge arises because flexural deformation in these layered structures is inevitably accompanied by interlayer sliding [13–16]. Consequently, a pivotal scientific question remains: how does interlayer sliding influence and potentially degrade/enhance the flexoelectric polarization and the resulting pseudo-piezoelectric response? Addressing this question is essential for optimizing the performance and reliability of next-generation 2D electronic devices.

Current research on flexoelectric applications primarily focuses on modulating the piezoelectric effect and ferroelectric polarization [17], as well as the flexoelectric photovoltaic effect [18,19]. Materials involved in these studies include $MoTe_2$ [3], $BaTiO_3$ [17], MoS_2 [18], and $CuInP_2S_6$ [19], among others. However, less attention has been paid to experimentally understanding the flexural deformation-induced phenomena in the 2D materials with sliding effects. To investigate the influence of interlayer sliding on flexoelectricity, non-piezoelectric materials should be selected to avoid coupling between piezoelectric and flexoelectric effects in the signals. Additionally, comparing materials with identical composition but differing structures—specifically layered versus nonlayered—is particularly crucial. $FeTe_x$ (x = 1 and 2) compounds belong to the transition metal chalcogenides (TMCs), exhibiting rich phase structures (layered and non-layered) and electronic properties and have consequently attracted considerable attention [20,21].

In this work, we grew high-quality FeTe [22–25] (centrosymmetric P4/nmm space group containing spatial inversion symmetry) stacked layers held by van der Waals forces, and $FeTe_2$ [26–29] (*Pnnm* space group) with a 3D network of edge-sharing and corner-sharing octahedra, as the ideal platform to understand the effects of interlayer sliding on the flexoelectricity. We reveal that interlayer sliding in layered FeTe causes an anomalous nonlinear pseudo-piezoelectric response and decay in polarization strength beyond a critical strain gradient, whereas nonlayered $FeTe_2$ maintains a linear response. Furthermore, we construct a deep-learning model to simulate the deformation characteristics of the system under bending. Models based on first-principles calculations help to identify the optimal sliding direction and elucidate the physical origin of the piezoelectric effect in the system. These findings provide crucial insights into controlling sliding-induced depolarization and offer practical guidelines for designing reliable flexoelectric and piezoelectric devices in 2D materials.

2. Results and discussion

1. Structure characterization of $FeTe_x$ nanosheets grown by the concentration gradient method

Fig. 1(a) presents a schematic illustration of our Chemical vapor deposition (CVD) method based on concentration gradient control. Unlike conventional CVD approaches [30,31], our method introduces distance as a key physical variable to regulate the Te vapor concentration, thereby enabling the synthesis of multiple compounds with different stoichiometries within a single experimental run. Under optimized conditions, we achieved the simultaneous growth of FeTe and $FeTe_2$ nanosheets in their respective temperature zones.

Fig. 1(b) and (c) display the optical microscopy (OM) images of $FeTe_x$ nanosheets grown on SiO_2/Si substrates. Fig. 1(b) shows FeTe nanosheets grown in the downstream region, where a lower Te vapor concentration resulted in a lower Te content (FeTe). Fig. 1(c) presents $FeTe_2$ nanosheets obtained under a higher Te vapor concentration. FeTe synthesized by the concentration gradient method exhibits regular tetragonal shapes, whereas $FeTe_2$ presents hexagonal morphologies. Since the morphologies of the FeTe and $FeTe_2$ nanosheets are determined by their crystal structures, the tetragonal and hexagonal shapes of FeTe and $FeTe_2$ imply their different crystal structures and symmetries. It is worth mentioning that, in our experiment, the key parameters for tuning the $FeTe_x$ crystal phases are the distance between the two precursors and the temperature [20] (See Fig.S1 for details of temperature-dependent growth of FeTex nanosheets), and therefore, the synthesis of $FeTe_x$ nanosheets with different phases and morphologies can be achieved by precisely regulating these two parameters.

Atomic force microscopy (AFM) morphology characterization on the as-grown $FeTe_x$ nanosheets shows that the FeTe nanosheet has a thickness of 9.7 nm, while the $FeTe_2$ nanosheet has a thickness of 9.8 nm. These results confirm that the concentration gradient method enables the synthesis of $FeTe_x$ nanosheets with a few nanometers in thickness. As shown in Fig. 1(f) and (g), Scanning electron microscope (SEM) and corresponding energy dispersive spectroscopy (EDS) mapping analyses further confirm the elemental distribution of FeTe and $FeTe_2$, consistent with the XPS analysis presented in Fig. S2. Both samples exhibit uniform elemental distributions in EDS elemental maps without defects, confirming the high-quality synthesis achieved by the concentration gradient method. Interestingly, the EDS and XPS results confirm that our FeTe nanosheets exhibit a slightly Fe-rich stoichiometry, while the $FeTe_2$ nanosheets maintain an ideal 1:2 ratio.

Raman spectroscopy was performed to investigate the lattice vibrations of $FeTe_x$, with the results presented in Fig. 1(h) and (i). The FeTe nanosheet exhibits characteristic peaks at 118 and 138 cm^{-1}, corresponding to its E_g and A_{1g} modes, while the $FeTe_2$ nanosheet shows peaks at 135 and 155 cm^{-1}, corresponding to its B_{1g} and A_g modes, in good agreement with previous reports [20,27]. Notably, as illustrated in Fig. S3, excessive Raman laser power can decompose $FeTe_2$ into Te, obscuring the intrinsic characteristic peaks. Further analysis of the Raman spectra will be discussed in detail later. In X-ray diffraction (XRD) patterns (Fig. 1(j) and (k)), all diffraction peaks of FeTe and $FeTe_2$ match well with the reference Powder Diffraction File (PDF) cards, confirming their phase purity. The sharp peaks with narrow full-width at half maximum indicate the good crystal quality of $FeTe_x$ nanosheets synthesized by the concentration gradient method. The (00l) diffraction peaks of FeTe confirm a layered structure with the c-axis out-of-plane, while the dominant (200) peak of $FeTe_2$ indicates its [100] direction is also out-of-plane. According to the XRD results, the schematic structural models are shown in Fig. 1(l) and (o), where FeTe crystallizes in the *P4/nmm* space group with van der Waals-coupled FeTe layers and Fe atoms centered in Te tetrahedra, while $FeTe_2$ adopts a nonlayered *Pnnm* structure featuring Fe-centered octahedra and Te_2^{2-} dimers. Fig. 1(m) and (p) present typical high-resolution transmission electron microscopy (HRTEM) images of the FeTe (along the [001] zone axis) and

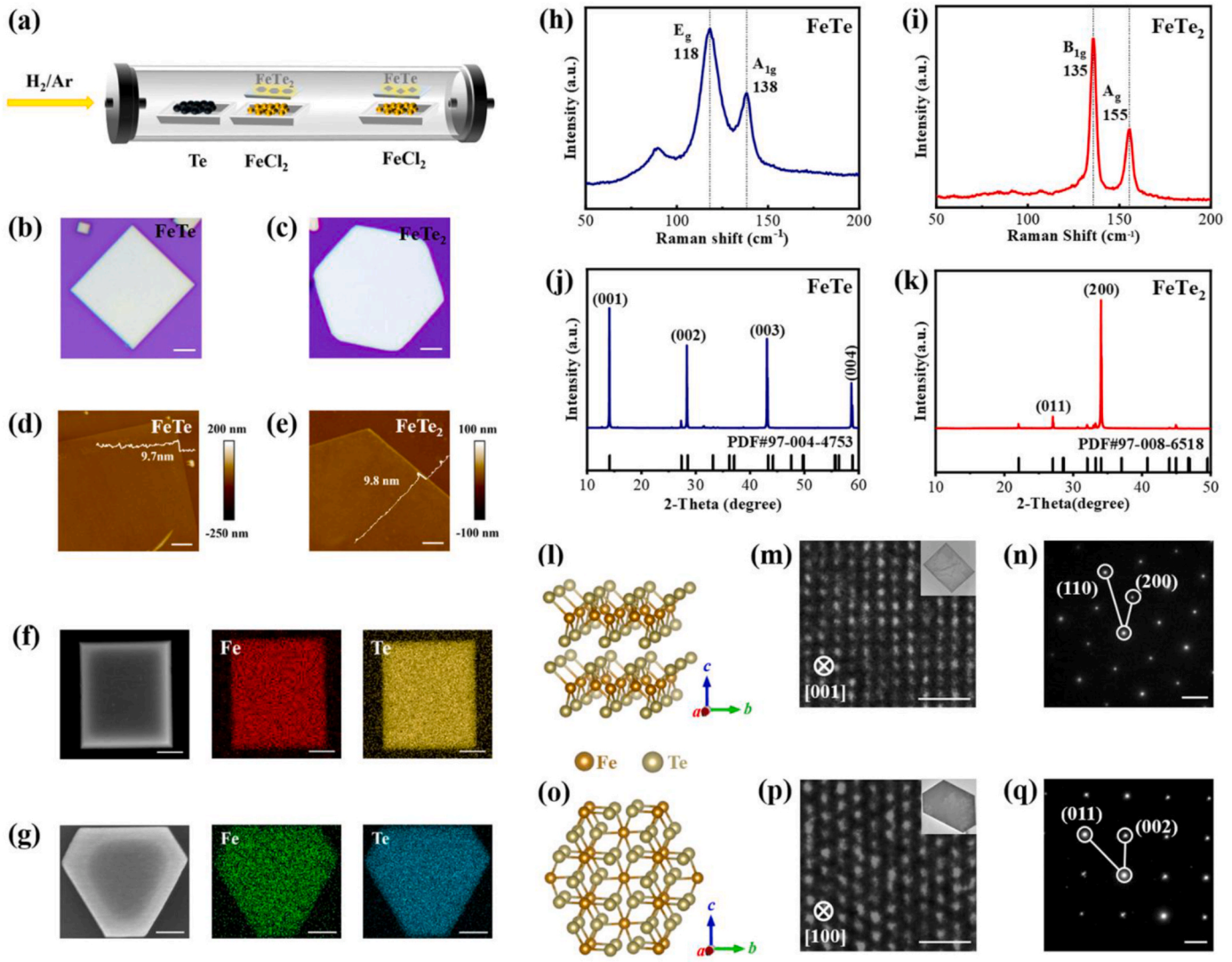

Fig. 1. The synthesis and structure characterization of $FeTe_x$ nanosheets. (a) Schematic illustration of the CVD synthesis of $FeTe_x$ using the concentration gradient method (near/far $FeCl_2$ correspond to $FeTe_2$/FeTe growth, respectively). (b, c) Optical microscopy (OM) images of FeTe and $FeTe_2$. Scale bars: 5 μm. (d, e) AFM topography images and corresponding height profile analysis of FeTe (Scale bars: 5 μm) and $FeTe_2$ (Scale bars: 1 μm). (f, g) SEM images and corresponding EDS mapping images of Fe and Te for FeTe (Scale bars: 2 μm) and $FeTe_2$ (Scale bars: 1 μm). (h, i) Raman spectra of FeTe and $FeTe_2$. (j, k) XRD spectra and corresponding standard PDF cards of FeTe and $FeTe_2$. (l, o) Schematic diagram of atomic structures of FeTe and $FeTe_2$. (m, p) HRTEM images of FeTe (Scale bars: 1 nm) and $FeTe_2$ (Scale bar: 1 nm) crystals. Insets: corresponding low-magnification TEM images (n, q) Corresponding SAED patterns captured from the random positions in FeTe (Scale bar:2 nm^{-1}) and $FeTe_2$ (Scale bar:2 nm^{-1}) nanosheets.

$FeTe_2$ (along the [100] zone axis) crystals, respectively. No discernible extended defects are observed in these HRTEM images, confirming the high crystallinity of the as-grown $FeTe_x$ nanosheets. Selected-area electron diffraction (SAED) patterns taken from random locations on the FeTe and $FeTe_2$ nanosheets (Fig. 1(n) and (q)) yield lattice constants in good agreement with the HRTEM results. Overall, the distinct phases yet compositionally similar characteristics make $FeTe_x$ an ideal platform for investigating the role of interlayer sliding in flexoelectricity and pseudo-piezoelectricity.

2. Generation of strain gradient and Raman peak shifts in suspended $FeTe_x$ nanosheets

Strain gradients in 2D materials can be achieved indirectly through specialized substrates [32], such as suspending 2D materials on rigid substrates with specific architectures [33,34], or flexible substrates with pretension [35–37]. Among these, the suspended circular drum model for strain induction has become a well-established technique, enabling quantitative measurement of mechanical properties across a wide range of 2D materials [32,38,39]. Here, the target substrate with 4 μm-diameter circular holes was fabricated on silicon wafers using photolithography and ion beam etching (IBE). Then, the CVD-grown $FeTe_x$ nanosheets were transferred from SiO_2/Si substrates to the target substrate (see detailed transfer process in Fig. S4 and the experimental section). Fig. 2(a) and (b) show OM images of the transferred FeTe and $FeTe_2$ nanosheets. Fig. 2(c) illustrates the strain gradient generation during the baking process [37]. After the nanosheets are transferred, residual solvent and water in the PS film evaporate, causing the PS layer to contract and exert a force on the nanosheet. This generates the pretension and establishes a spatial strain gradient inside the nanosheets.

Raman spectroscopy was employed to monitor the evolution of surface lattice deformation in $FeTe_x$ nanosheets under varying degrees of bending. After sample transfer, the $FeTe_x$ nanosheet covers the circular aperture on the substrate, leaving its center suspended. The pretension generated during the sample transfer introduces a strain

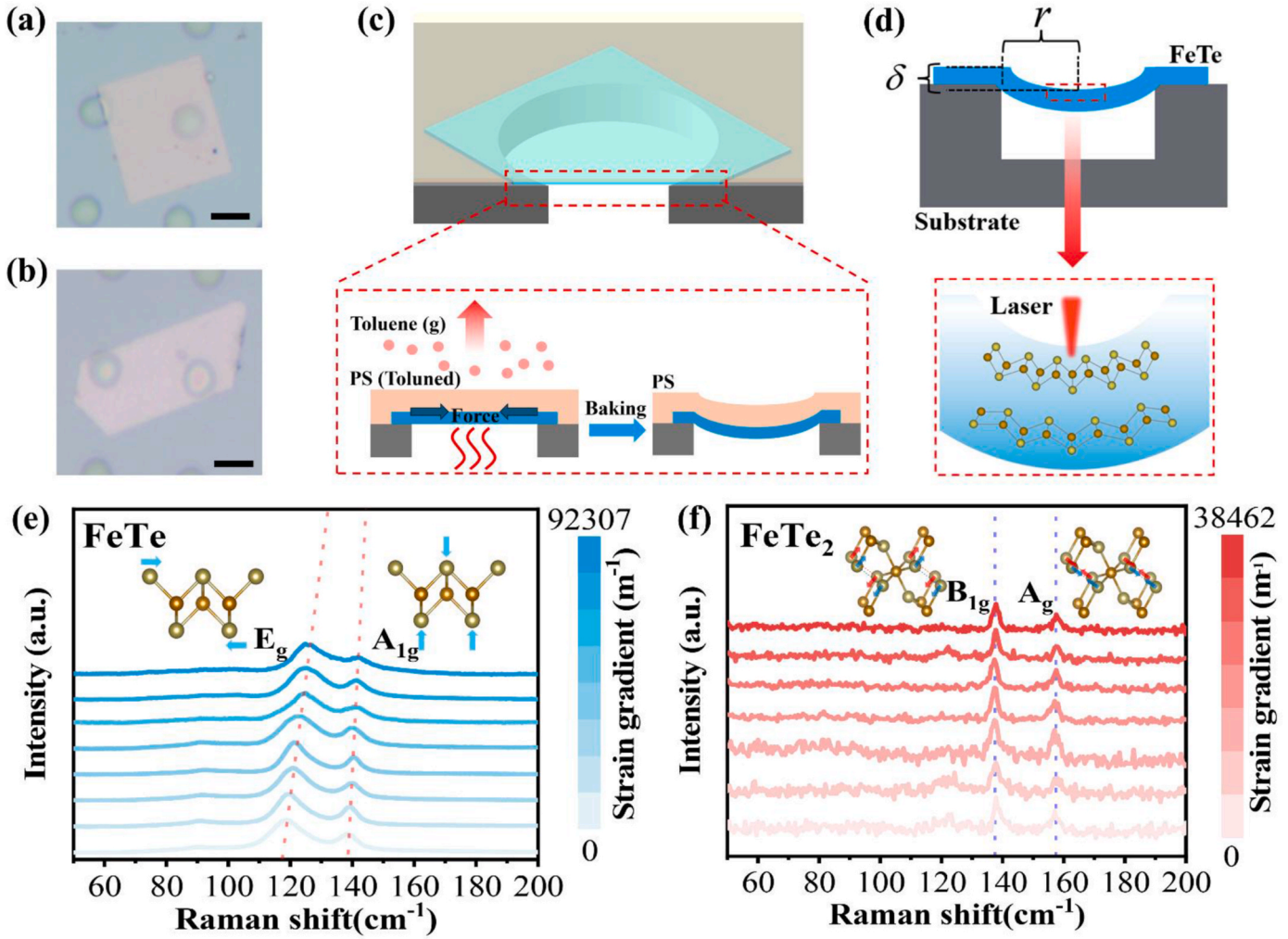

Fig. 2. Strain gradient generation of suspended $FeTe_x$ nanosheets and Raman characterization with controlled aspect ratio. (a, b) OM images of transferred FeTe and $FeTe_2$ nanosheets. Scale bars: 5 μm. (c) Illustrations of the strain gradient generation during the baking process. (d) Illustration of the cross-sectional view of suspended FeTe nanosheets with pretension. The red dashed line indicates the schematic configuration of the Raman characterization of the deformed FeTe. (e, f) Raman spectra of FeTe and $FeTe_2$ nanosheets (20-30 nm) deformed with different strain gradients.

gradient. Taking FeTe as an example, Fig. 2(d) shows the cross-sectional profile of the suspended FeTe nanosheet, where r denotes the hole radius and δ denotes the central deflection. For the nanosheet with a given thickness, the degree of bending is determined by the pretension and can be characterized by the aspect ratio (δ/r [40]). In addition, the aspect ratio can be converted into the strain gradient through the membrane curvature ($k \approx 2\delta/r^2$ for the spherical-cap geometry), which quantitatively characterizes the bending state of the nanosheet. The dashed box in Fig. 2(d) indicates the schematic configuration of the Raman characterization of the deformed FeTe. When the FeTe nanosheet bends, its local atomic structure is correspondingly modified. Variations in chemical bond lengths and angles alter the lattice vibrations, and these changes can be analyzed by Raman spectroscopy [41]. Fig. 2(e) and (f) present the Raman spectra of FeTe and $FeTe_2$ nanosheets under different strain gradients. The Raman spectrum of FeTe exhibits two characteristic vibrational modes: E_g mode at 118 cm^{-1} and A_{1g} mode at 138 cm^{-1}, which vibrate along in-plane and out-of-plane directions, respectively [42]. It is found from Fig. 2(e) that, with the increase of strain gradients from 0 to 92307 m^{-1}, the Raman peaks show a certain degree of shift (Δ_{shift} = 5.9 and 2.7 cm^{-1} for the peaks at 118 and 138 cm^{-1}, respectively). However, for $FeTe_2$ nanosheets, such a Raman peak shift is negligible. $FeTe_2$ exhibits two characteristic vibrational modes: B_{1g} mode at 135 cm^{-1} and A_g mode at 155 cm^{-1}, as shown in Fig. 2(f), where the former is attributed to the liberational modes and the latter corresponds to the Te-Te stretching modes [43]. The two characteristic Raman peaks of $FeTe_2$ remain stable as the strain gradient varies from 0 to 38462 m^{-1}, suggesting that the pretension-induced lattice deformation is not strong enough to be detected by our Raman spectroscopy. Interestingly, we found that the pretension introduced by the sample transfer can only generate a maximum strain gradient of 38462 m^{-1} in the $FeTe_2$ nanosheet, which is likely attributable to the three-dimensional crystal structure of $FeTe_2$ that has high mechanical rigidity which can resist changes in bond length and bond angle.

3. Revealing the nanomechanical properties of $FeTe_x$ nanosheets and interlayer sliding via AFM-based nanoindentations

To better elucidate the mechanical properties of FeTe and $FeTe_2$, we employed AFM nanoindentation to investigate the mechanical response of the suspended FeTe and $FeTe_2$ nanosheets. As shown in Fig. 3(a), by pressing the AFM tip onto the sample surface under controlled forces and monitoring the resulting deformation, the mechanical characteristics of the sample can be extracted. Fig. 3(b) and (c) present the AFM topography images of FeTe and $FeTe_2$ nanosheets on the substrate. The surfaces exhibit no observable wrinkles or cracks, demonstrating that the transfer method achieves damage-free transfer. Fig. 3(d) and (e)

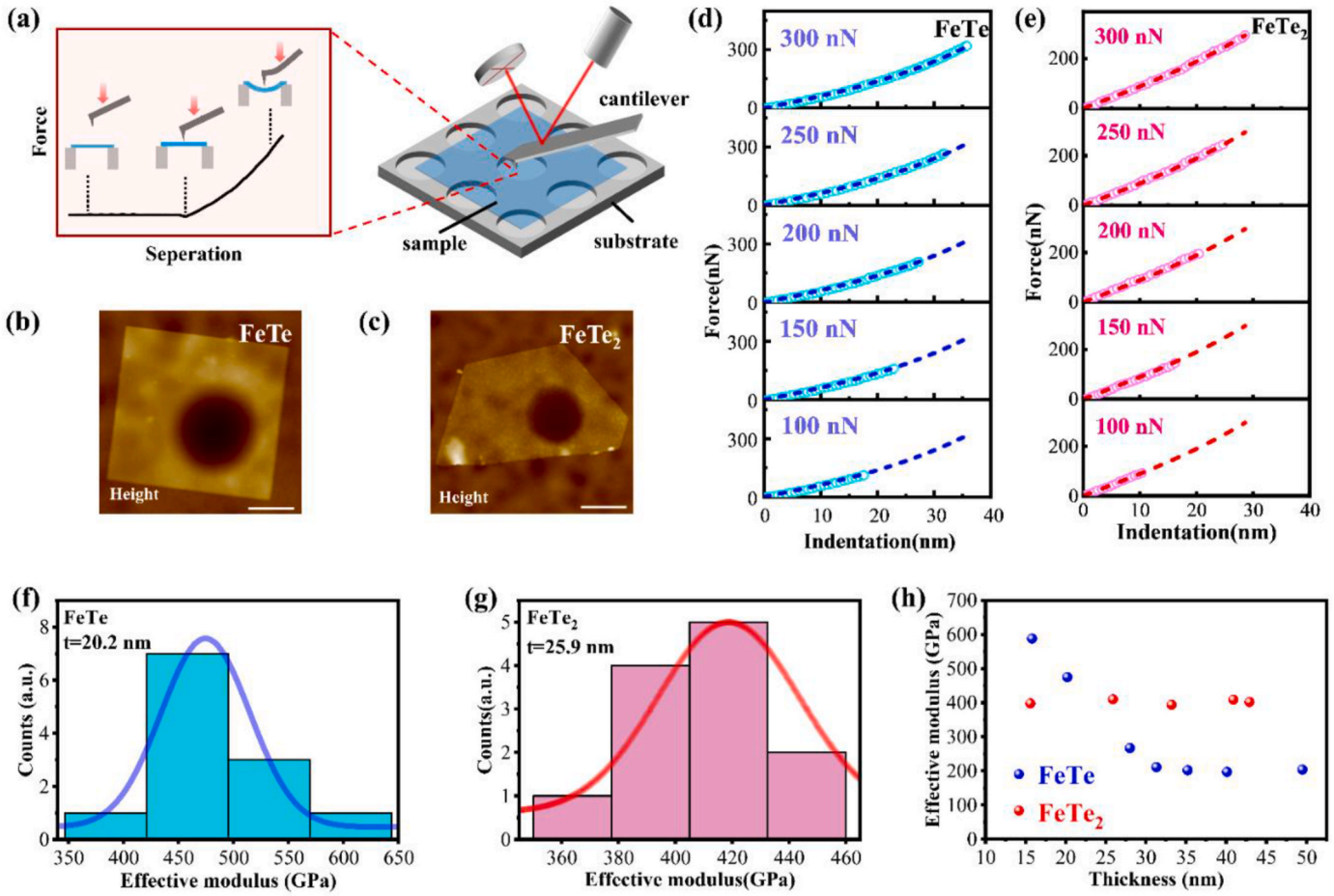

Fig. 3. AFM nanoindentation test for elastic properties of $FeTe_x$ nanosheets. (a) Illustration of AFM nanoindentation test. (b, c) AFM topography images of the FeTe and $FeTe_2$ nanosheets. Scale bars: 2 μm. (d, e) Five consecutive force-indentation curves of FeTe and $FeTe_2$ under different force set-points. The dashed lines are fitting curves. (f, g) Histograms of the measured effective modulus for FeTe (20.2 nm) and $FeTe_2$ (25.9 nm) nanosheets. The solid lines represent the fitting result based on a Gaussian distribution. (h) Thickness dependence of Young's modulus graph of $FeTe_x$ nanosheets.

show five consecutive force-indentation curves of $FeTe_x$ under different forces (from 100 n*N* to 300 n*N*). Five curves exhibit exceptional consistency and reproducibility. Notably, all data in Fig. 3 were obtained within the reversible elastic deformation range of the $FeTe_x$ nanosheets. Excessive force may cause plastic deformation and eventual fracture (Fig. S5). To derive the Young's modulus, the deformation at the center of $FeTe_x$ nanosheets can be reasonably considered as an elasticity using a continuum mechanical model [44]. Under the aforementioned conditions, the force-indentation relation can be expressed as: $F = \left[\frac{4\pi E}{3(1-\nu^2)}\left(\frac{t^3}{r^2}\right)\right]\delta + (\pi T)\delta + \left(\frac{Eq^3t}{r^2}\right)\delta^3$ [45], where E and T are elastic modulus and pretension of sample, t and r denote the thickness of sample and radius of hole, and q is a dimensionless constant determined by Poisson's ratio (ν) of sample, obeying $q = 1.05 - 0.15\nu - 0.16\nu^2$ [46]. Based on the above equation, the fitting curve (dashed lines) in Fig. 3(d) and (e) can be obtained, which show good agreement with the experimental data. We further plotted the histogram of all effective modulus results (Fig. 3(f and g)) obtained from the two FeTe (20.2 nm) and $FeTe_2$ (25.9 nm) nanosheets, which well follow a Gaussian distribution with peak center positions of 475 and 418 GPa, respectively.

Nanomechanical measurements were further performed on samples with varying thicknesses (force-indentation curves of $FeTe_x$ nanosheets with different thicknesses under 300 n*N* are shown in Fig. S6). The results are summarized in Fig. 3(h). The Young's modulus of FeTe nanosheets exhibits a distinct thickness dependence, decreasing monotonically with increasing thickness until reaching a saturation value of ~197 GPa at around 31 nm. In contrast, $FeTe_2$ maintains an average modulus of ~401 GPa in the thickness range of interest. This may originate from their fundamentally different interlayer interactions: the mechanical properties of $FeTe_2$ are dominated by covalent bonding, while FeTe shows thickness-dependent mechanics analogous to black phosphorus [47,48], where interlayer sliding via van der Waals forces enables thickness-dependent energy minimization. It has been reported that interlayer sliding, a common phenomenon in 2D van der Waals materials, disrupts the conventional flexoelectric-related effect by introducing a highly localized and non-uniform shear strain gradient at the van der Waals interface [14]. This may alter the symmetry breaking of ionic charge centers, potentially modulating the polarization strength through an additional sliding-induced dipole moment [14], making its understanding critical for accurately modelling and harnessing mechanical-electrical coupling properties in layered material systems.

4. Interlayer sliding induced non-linear pseudo-piezoelectric response in suspended $FeTe_x$ nanosheets

Nanoindentation characterizations demonstrate that interlayer sliding can modulate mechanical behavior. Since flexoelectricity arises from stress-induced strain gradients introduced by bending deformation, such sliding is expected to affect flexoelectric effects as well. As exemplified by FeTe (Fig. 4(a)), the stress applied to the FeTe nanosheet generates strain gradients that can break charge and lattice structure symmetries. The resultant polarization can be detected by measuring the

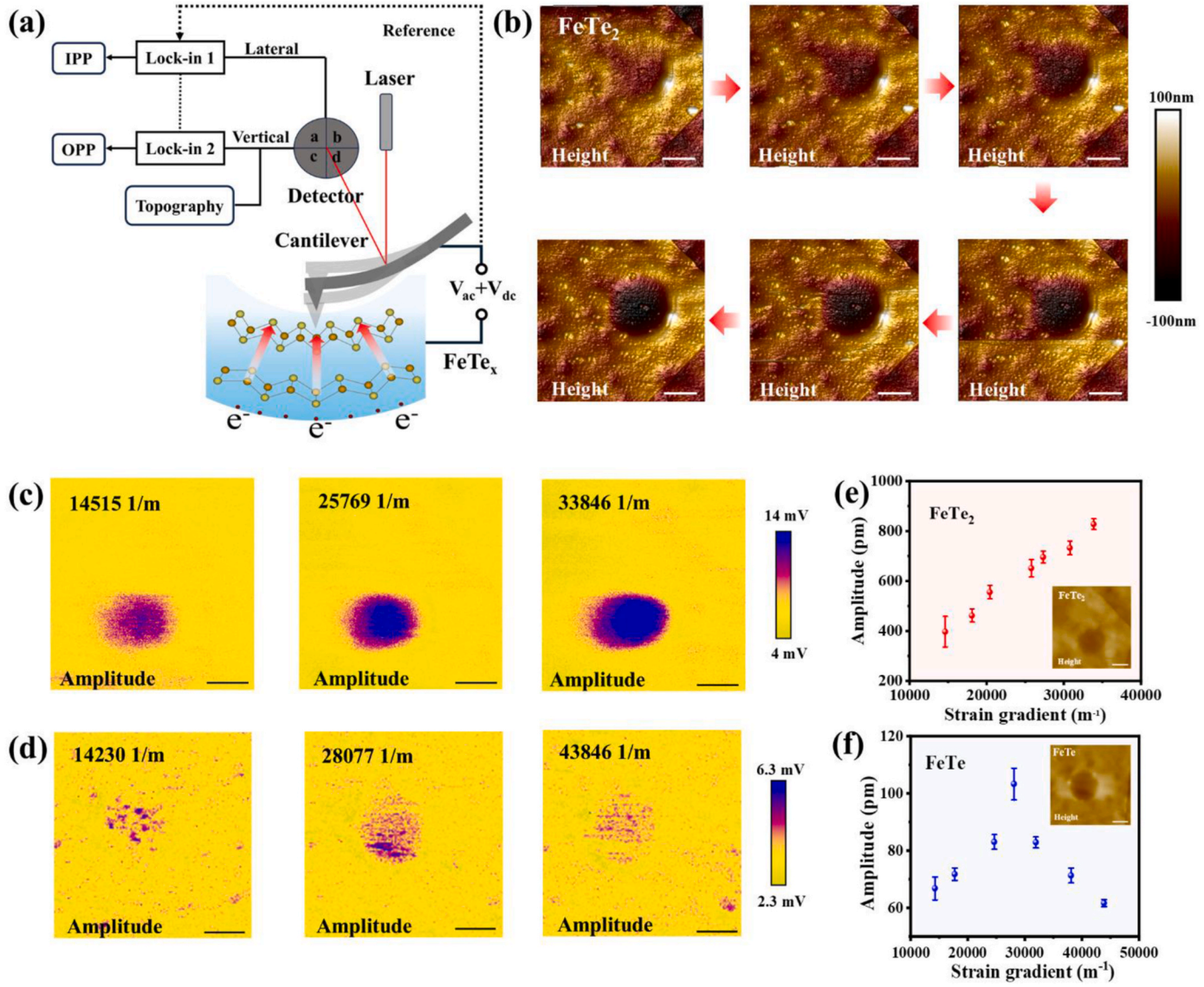

Fig. 4. Generation of flexoelectric polarization under various strains in suspended $FeTe_x$ nanosheets. (a) Illustration of PFM characterization of FeTe nanosheets under a tip-induced force (the red arrows indicate the polarization direction). (b) A typical 3D AFM topographic image of elastically deformed suspended FeTe nanosheets under different forces. Scale bars:2 μm. (c) PFM amplitude of $FeTe_2$ under different applied strain gradients. The applied strain gradient increases from 14515 m^{-1} to 33846 m^{-1}. Scale bars: 2 μm. (d) PFM amplitude of FeTe under different applied strain gradients. The applied strain gradient increases from 14230 m^{-1} to 43846 m^{-1}. Scale bars: 2 μm. (e, f) PFM amplitude at the center of suspended $FeTe_2$ nanosheets and suspended FeTe nanosheets with different strain gradients (insets are the corresponding topographic images of suspended $FeTe_2$ and FeTe ultrathin nanosheets (1.1-1.3 nm). Scale bars: 2 μm).

electromechanical response to an applied AC voltage (V_{ac}) through PFM, generating the pseudo-piezoelectric effect.

We used PFM to characterize the polarization behavior of suspended ultrathin FeTe and $FeTe_2$ nanosheets under different tip-induced deformations. Fig. 4(b) shows a representative topographic image of suspended nanosheets during forces increasing from about a few n*N* to about 1000 n*N*. The PFM amplitude responses of ultrathin $FeTe_2$ and FeTe nanosheets under various applied strain gradients (obtained from the membrane curvature determined from the AFM cross-sectional profiles) are shown in Fig. 4(c) and (d) (see Figs. S7 and S8 for details). It is worth noting that, since FeTe is metallic in its bulk form, the pseudo-piezoelectric response could be only observed in the ultrathin and slightly non-stoichiometric FeTe nanosheets in our experiments. For the suspended ultrathin $FeTe_x$ nanosheets, the established proportional relationship between polarization and tip oscillation amplitude in ferroelectric materials remains valid for their pseudo-piezoelectric response [49,50].

To better visualize the evolution process of $FeTe_x$ nanosheets under different strain gradients, we summarize the amplitude (polarization) variations for both layered FeTe and nonlayered $FeTe_2$ in Fig. 4(e) and (f). PFM characterization of nonlayered $FeTe_2$ nanosheets demonstrates that the amplitude (polarization) increases monotonically with the strain gradient. However, the experimental results for FeTe nanosheets exhibit fundamentally different behavior from that of $FeTe_2$ nanosheets. When the applied strain gradient is below ~28077 m^{-1}, the amplitude (polarization) rises with increasing strain gradient, but the amplitude (polarization) begins to decrease as the applied strain gradient exceeds the critical point. Considering that FeTe and $FeTe_2$ are both composed of Fe and Te and exhibit neither piezoelectricity nor ferroelectricity, their distinct polarization behaviors originate solely from their different crystal structures in response to the flexural deformation.

$FeTe_2$ adopts a nonlayered structure with a three-dimensional rigid lattice that lacks interlayer sliding degrees of freedom, hence, its polarization under external force arises exclusively from lattice distortions

induced by strain gradients, resulting in a monotonic increase in polarization with increasing distortion. In contrast, FeTe possesses a layered van der Waals structure with relatively weak interlayer coupling, thereby enabling interlayer sliding. The applied force not only induces lattice distortion in FeTe to generate flexoelectric polarization but may also trigger interlayer sliding that may modify the stacking configuration, consequently weakening the net polarization. Additionally, interlayer sliding can disrupt the linear proportionality between polarization and macroscopic strain gradient, as nonlinear, friction-dependent processes such as stick-slip motion become dominant in the high-deformation region [51,52]. As a result, it is observed in Fig. 4(f) that under small strain gradients, pseudo-piezoelectricity dominates the polarization of FeTe, yielding an increasing trend like that of $FeTe_2$; however, once the strain gradient exceeds a threshold, interlayer sliding may be activated: without vertical ion displacement, a lateral interlayer shift alone suffices to modify the stacking sequence and lead to a decay in the measured amplitude signal [50].

5. Atomic-scale mechanisms of interlayer sliding and insights for 2D electronic fabrication

The flexoelectric polarization in FeTe arises from the strain gradient induced by bending deformation, which breaks spatial inversion symmetry. To elucidate the microscopic structure and molecular dynamics of the flexed system, we trained a neural network (NN) interatomic potential to model bilayer FeTe under bending deformation (Fig. 5). The learning curves, represented by the root mean square errors (RMSE) of the energy and atomic forces for the validation set as functions of the training steps, are shown in Fig. 5(d). Molecular dynamics simulations were then performed using this machine-learned potential. A 15×15 bilayer FeTe supercell and its schematic representation are shown in Fig. 5(a) and (b), respectively. The aspect ratio of the model is set to 0.192 to approximate the experimentally observed degree of bending. At the atomic level, the bending deformation induces relative sliding between the FeTe layers, resulting in different stacking configurations such as BA, AA and AB. Fig. 5(c) presents cross-sectional views of the flexed structure along the [100] and [010] directions, revealing the bending-

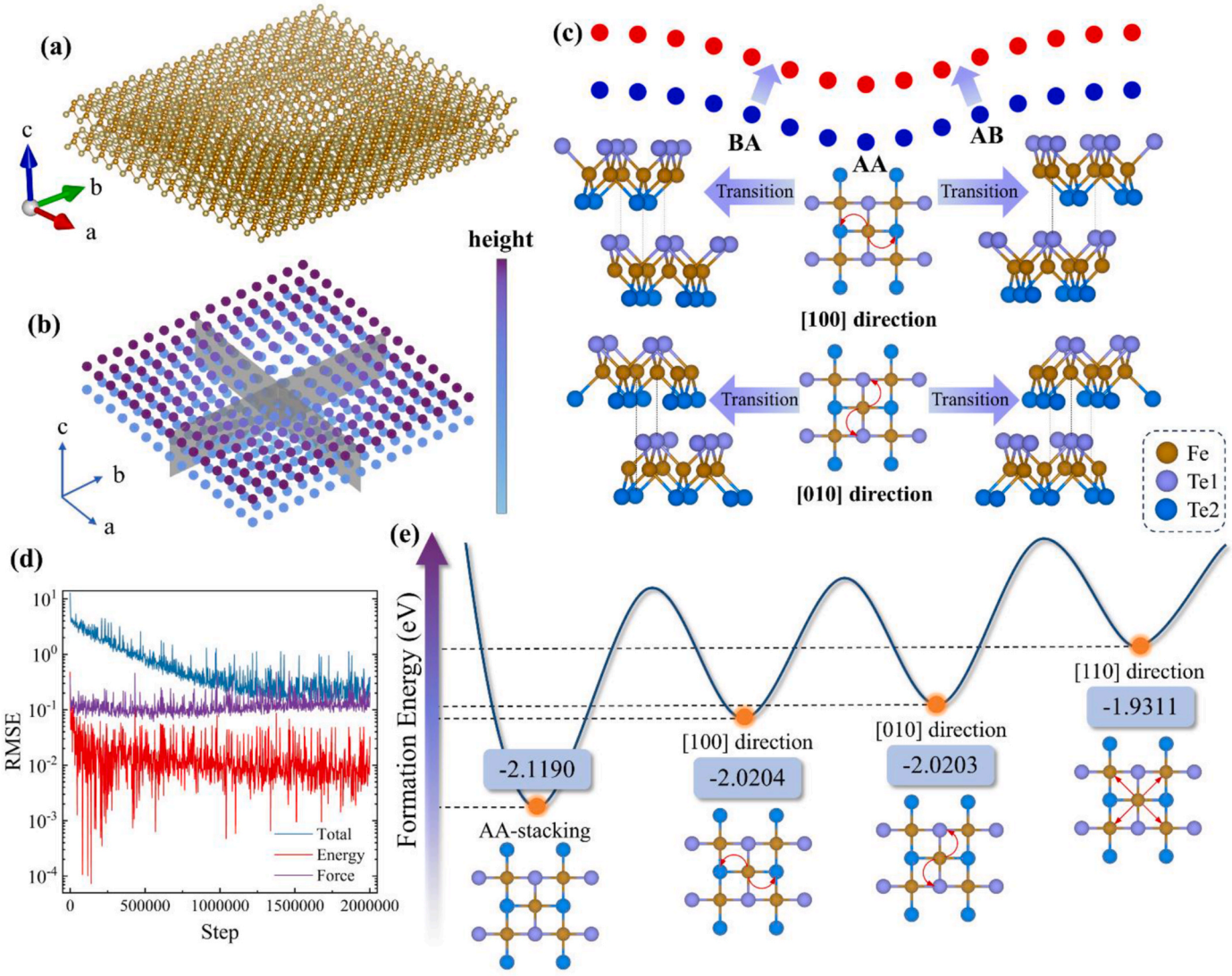

Fig. 5. (a) Structure of a bilayer flexed FeTe supercell with a size of 15 × 15. (b) Simplified schematic in which each FeTe unit cell is represented by a single point. (c) Cross-sectional schematic along the [100] or [010] direction in panel (b) illustrating the switching among AB, AA, and BA stacking configurations induced by relative interlayer sliding during bending deformation. Te atoms in different Wyckoff positions are shown in blue and purple. Red arrows indicate the sliding direction. (d) Learning curves of the machine-learning interatomic potential model. (e) Atomic structures of FeTe under interlayer sliding along different directions and the corresponding formation energies.

induced sliding process. Compared with sliding along the diagonal [110] direction, sliding along the [100] or [010] direction exhibits a lower formation energy (Fig. 5(e)), indicating that interlayer sliding preferentially occurs along the crystal edges (the [100] or [010] direction) rather than along the diagonal ([110] direction) in flexurally deformed FeTe single-crystal nanosheets. Notably, inversion symmetry is preserved in the FeTe bilayer after interlayer sliding along both the [100] and [010] directions (Fig. S9). Since flexural deformation often occurs at the contact regions between the channel nanosheet and the drain (or source) electrodes in 2D transistors, the resulting flexoelectric polarization may affect electron transport across the drain—source interface. This insight suggests that the polarization field strength at the channel—drain/source contact, and hence the contact barrier, can be tuned by adjusting the stacking orientation of the channel nanosheet in the transistor architecture. Furthermore, the unique polarization characteristics of FeTe offer new material design strategies for emerging applications such as neuromorphic computing [53] (emulating synaptic weight modulation) and dual-channel sensing units [54] (enabling sensitivity mode switching).

3. Conclusion

This study demonstrates that interlayer sliding critically determines the flexoelectric performance of 2D materials under bending. While nonlayered $FeTe_2$ exhibits a stable, linear electromechanical response ideal for strain-gradient engineering, layered FeTe shows a nonlinear and decaying response due to interlayer sliding, which dissipates the necessary strain gradient. Our combined experiments and simulations reveal that sliding preferentially occurs along [100] crystallographic axes in FeTe, directly linking atomic-scale motion to macroscopic function. These findings establish interlayer sliding as a key design parameter for 2D flexible electronics. For reliable flexoelectricity, materials with strong intralayer bonding and slip resistance are superior. Furthermore, controlling the stacking orientation of layered materials offers a viable strategy to tune interfacial polarization and contact barriers, providing a new design principle for adaptive electronic devices.

4. Methods

4.1. Experimental section

$FeTe_x$ nanosheets Growth (concentration gradient method): $FeTe_x$ nanosheets were synthesized in a dual heating zone tube furnace using Te powder and $FeCl_2$ powder as precursors under an Ar/H_2 (10:1) mixed atmosphere. The precursors were precisely weighed at a 1:4 molar ratio (Te: $FeCl_2$), loaded into quartz boats, and arranged according to the configuration shown in Fig. 1(a). By systematically varying the spatial separation between the $FeCl_2$ powder and Te powder, we established a controllable Te concentration gradient in the gas flow, which critically determines the phase of the nanosheets. Under optimized conditions with $FeCl_2$ powder positioned at 8 cm (upstream) and 40 cm (downstream) from the Te powder, with a growth time of 3-5 min and growth temperatures of 570°C (upstream) and 610°C (downstream). This approach differs from conventional CVD by employing distance as a key physical variable to control Te vapor concentration, enabling the synthesis of multiple compounds with varying stoichiometries in a single experiment. Notably, this strategy is not limited to $FeTe_x$—it can be extended to other multiphase compounds, reducing material preparation time. In this experiment, SiO_2/Si substrates were selected instead of mica substrates due to their significantly lower cost, making them more practical for large-scale research applications. The SiO_2/Si substrates exhibit excellent chemical inertness and thermal stability at high temperatures, while their atomically flat surface promotes uniform nucleation and continuous growth of 2D materials.

Characterization: X-ray diffraction (XRD) patterns were collected using a Rigaku Mini-Flex II diffractometer with Cu Kα radiation ($\lambda = 1.5406$ Å). Energy dispersive X-ray spectroscopy (EDS) was performed on a Hitachi SU-8010 scanning electron microscope. Raman spectra were acquired at room temperature using a HORIBA JobinYvon Evolution spectrometer equipped with a 532 nm laser. L-TEM imaging was carried out on a JEM-F200 (JEOL) transmission electron microscope at an accelerating voltage of 200 kV, with the specimens maintained at room temperature throughout the observation. Atomic force microscopy (AFM) characterization was conducted on a Bruker Dimension Icon system. Notably, all AFM tests were carried out inside a glovebox to minimize interference from external environmental fluctuations. The PFM measurements were performed using Bruker SCM-PIT-V2 probes (antimony-doped n-type Si cantilever with a conductive Pt/Ir coating). The nominal tip radius is 25 nm, the spring constant is ~3 N/m, and the resonance frequency is ~75 kHz. SEM characterization of the probe is provided in Supplementary Fig. S10.

Transfer of $FeTe_x$ nanosheets (surface energy assisted transfer method): Polystyrene (PS) dissolved in toluene was selected as the hydrophobic polymer material. The PS solution was uniformly deposited via spin-coating, followed by baking to evaporate the toluene solvent. The edges of PS/FeTe/SiO_2 were scratched with a width of ~0.5 mm to expose the hydrophilic substrate surface. The substrate was then tilted and immersed in deionized water to facilitate PS film detachment, which was subsequently retrieved using the porous substrate. After tilting and standing to remove residual water between the PS film and the new substrate, thermal baking was performed to enhance interfacial adhesion. After cooling to room temperature, the PS layer was dissolved in toluene, and final cleaning was carried out in alcohol to complete the non-destructive transfer process.

4.2. DFT calculations

The bilayer model of FeTe was adopted as a simplified theoretical framework to investigate the fundamental interlayer sliding mechanism in FeTe and elucidate the underlying sliding-induced structural and energetic changes. Density functional theory (DFT) calculations were performed using the Vienna Ab initio Simulation Package (VASP) [55,56] with projector augmented-wave (PAW) potentials [57]. The Perdew-Burke-Ernzerhof (PBE) functional within the generalized gradient approximation (GGA) [58] was adopted to treat the exchange correlation potentials. The electronic calculations used a plane-wave energy cutoff of 350 eV. The FeTe structures and sliding configurations were fully relaxed until the residual force on each atom was less than 0.001 eV/Å, and the total energy convergence criterion was set to 10^{-8} eV. The Brillouin zone was sampled using a Γ-centered $9 \times 9 \times 1$ k-point mesh. Van der Waals interactions were taken into account using the DFT-D3 method [59]. To simulate the experimentally observed nonmagnetic state of FeTe at room temperature, magnetism was not considered in the calculations. The formation energy was calculated according to the following equation:

$$E_{\text{form}} = E_{\text{tot}} - n_{\text{Fe}}\mu_{\text{Fe}} - n_{\text{Te}}\mu_{\text{Te}}$$

where E_{tot} is the Helmholtz free energy of the system of n_X atoms of element X with the corresponding chemical potential μ_X, where $X =$ Fe, Te.

4.3. Machine learning

3943-step AIMD simulations were conducted to generate training datasets utilizing the VASP package. 394 steps of the training data were used for validation. The sizes of the embedding and fitting networks include three hidden layers, are (25, 50, 100) and (240, 240, 240), respectively. The cutoff radius of the model was set to 6.0 Å for neighbor searching, while the smoothing function starts from 2.0 Å. Two million steps (batches) with a batch size of 1 were used to minimize the loss

function that includes energy and force contributions. The DEEPMD-KIT code was used to train of DP model [60,61]. The DP compression scheme was applied in this work to accelerate the computational efficiency of the DPMD simulations. The accuracy of the trained machine-learning interatomic potential was validated by the learning curves and parity plots shown in Fig. S11. The energy RMSE per atom was 0.02 eV. The force RMSE was 0.11 eV/Å. The NN potentials were used to relax the superlattice within the LAMMPS package until the maximum atomic force was smaller than 10^{-4} eV/Å [62]. The DPMD simulations started from bilayer flexed FeTe cell building blocks constructed using a 15×15 supercell.

CRediT authorship contribution statement

Jing Chen: Writing – original draft, Methodology, Investigation, Data curation. **Jiefeng Ye:** Writing – original draft, Software, Investigation. **Yifei Ma:** Investigation, Formal analysis. **Changlin Chen:** Software, Investigation. **Shangrun Lu:** Resources, Investigation. **Liwei Guan:** Writing – review & editing, Resources, Investigation. **Weijian Zhang:** Resources, Formal analysis. **Hongyi Lu:** Software, Formal analysis. **Zhongchong Lin:** Writing – review & editing, Resources, Project administration, Formal analysis. **Huaixi Chen:** Writing – review & editing, Validation, Resources, Data curation. **Guoyang Su:** Investigation, Data curation. **Yuling Zhou:** Software, Data curation. **Luis A. Montero-Cabrera:** Software, Resources. **Oleg V. Kolosov:** Resources, Formal analysis. **Licong Peng:** Resources, Investigation. **Liqiang Zeng:** Software, Investigation. **Ziyang Gan:** Project administration, Investigation. **Zixuan Cao:** Resources, Formal analysis. **Jianmin Zhang:** Writing – review & editing, Methodology, Formal analysis. **Yue Chen:** Writing – review & editing, Software, Investigation, Conceptualization. **Zhigao Huang:** Writing – review & editing, Software, Resources, Data curation.

Declaration of competing interest

The authors declare that they have no known competing financial interests or personal relationships that could have appeared to influence the work reported in this paper.

Acknowledgement

The authors wish to acknowledge the financial support from the National Natural Science Foundation of China (Nos. 62474041, 52403294, 52402183 and 52601337), the Natural Science Foundation of the Fujian Province (Nos. 2023J01521, 2025J09034), the National Key Research and Development Program of China (2025YFA1411002), Fu-Xia-Quan National Independent Innovation Demonstration Zone Collaborative Innovation Platform (2025QZFX02), State Key Laboratory of Functional Crystals and Devices Open Funding Project (SKLFCD202502F), National Laboratory Quantum Technology Instrument Project (2024YQ02001), the financial support from China Scholarship Council (202508350013), the Yuelushan Center for Industrial Innovation Projects (2025YCII0121), and the project PNCB (PN223LH010-081) of the Cuban Ministry of Science, Technology, and Environment.

Supporting information

Supporting Information is available from the Wiley Online Library or from the author.

Appendix A. Supplementary data

Supplementary data to this article can be found online at https://doi.org/10.1016/j.mtphys.2026.102297.

Data availability

Data will be made available on request.

References

[1] J. Narvaez, F. VasquezSancho, G. Catalan, Enhanced flexoelectric-like response in oxide semiconductors, Nature 538 (7624) (2016) 219.
[2] T.D. Nguyen, S. Mao, Y.W. Yeh, P.K. Purohit, M.C. McAlpine, Nanoscale flexoelectricity, Adv. Mater. 25 (7) (2013) 946.
[3] S. Kang, S. Jeon, S. Kim, et al., Tunable out-of-plane piezoelectricity in thin-layered $MoTe_2$ by Surface corrugation-mediated flexoelectricity, ACS Appl. Mater. Interfaces 10 (32) (2018): 27424.
[4] A. Coşkun, A.S. Kopar, Z.E. Özerbaş, et al., Experimental insights into characteristic properties and applications of two-dimensional Janus transition metal dichalcogenide (TMDC) materials: a comprehensive review, Rare Met. 44 (11) (2025) 8161.
[5] X. Wen, Q. Ma, A. Mannino, M. Fernandez Serra, S. Shen, G. Catalan, Flexoelectricity and surface ferroelectricity of water ice, Nat. Phys. 21 (2025) 1587.
[6] A. Riaz, K. Witte, W. Bodnar, E. Burkel, Pseudo-Piezoelectricity in calcium titanate: towards novel implant materials, Scr. Mater. 188 (2020) 274.
[7] A. Riaz, K. Witte, W. Bodnar, et al., Structural changes and pseudo-piezoelectric behaviour of field assisted sintered calcium titanate, Materialia 15 (2021): 100998.
[8] W. Zhu, J.Y. Fu, N. Li, L. Cross, Piezoelectric composite based on the enhanced flexoelectric effects, Appl. Phys. Lett. 89 (2006): 192904.
[9] B. Chu, W. Zhu, N. Li, L.E. Cross, Flexure mode flexoelectric piezoelectric composites, Appl. Phys. Lett. 106 (2009): 104109.
[10] L.Y. Deng, Q. Zhang, W.Y. Li, et al., KCl acts as a flux to assist the growth of sub-millimeter-scale metallic 2D non-layered molybdenum dioxide, Rare Met. 44 (1) (2024) 404.
[11] D. Guo, X.Y. Rui, S. Du, Q.R. Liang, H. Yang, S.J. Zheng, Emerging spintronics applications of magnetic van der Waals heterostructures, Rare Met. 44 (12) (2025) 9336.
[12] J. Očenášek, H. Lu, C.W. Bark, et al., Nanomechanics of flexoelectric switching, Phys. Rev. B 92 (3) (2015): 035417.
[13] Z. Guan, L. Wei, W. Fan, et al., Mechanical force-induced interlayer sliding in interfacial ferroelectrics, Nat. Commun. 16 (1) (2025) 986.
[14] R. He, H. Wang, F. Deng, et al., Sliding Flexoelectricity in Two-Dimensional van der Waals Systems, Microsyst. Nanoeng. 10 (2024) 151.
[15] K. Yasuda, E. Zalys-Geller, X. Wang, et al., Ultrafast high-endurance memory based on sliding ferroelectrics, Science 385 (6704) (2024) 53.
[16] X. Li, B. Qin, Y. Wang, et al., Sliding ferroelectric memories and synapses based on rhombohedral-stacked bilayer MoS2, Nat. Commun. 15 (1) (2024).
[17] H. Lu, C.W. Bark, D. Esque de los Ojos, et al., Mechanical writing of ferroelectric polarization, Science 336 (6077) (2012) 59.
[18] J. Jiang, Z. Chen, Y. Hu, et al., Flexo-Photovoltaic effect in MoS_2, Nat. Nanotechnol. 16 (8) (2021) 894.
[19] J. Yu, B. Huang, S. Yang, et al., Flexoelectric engineering of bulk photovoltaic photodetector, Nano Lett. 24 (21) (2024) 6337.
[20] M. Cheng, X. Zhao, Y. Zeng, et al., Phase-Tunable synthesis and etching-free transfer of two-dimensional magnetic FeTe, ACS Nano 15 (12) (2021): 19089.
[21] B.P. Jena, C. Sudakar, Micron-Sized 2D marcasite $FeTe_2$ nanocrystals for spintronics applications, ACS Appl. Nano Mater. 7 (22) (2024): 26215.
[22] X. Wang, C. Bian, Y. He, et al., Ultrathin FeTe nanosheets with tetragonal and hexagonal phases synthesized by chemical vapor deposition, Mater. Today 45 (2021) 35.
[23] L. Kang, C. Ye, X. Zhao, et al., Phase-controllable growth of ultrathin 2D magnetic FeTe crystals, Nat. Commun. 11 (1) (2020) 3729.
[24] H. Zhang, Q. Li, M. Hossain, et al., Phase-selective synthesis of ultrathin FeTe nanoplates by controllable Fe/Te atom ratio in the growth atmosphere, Small 17 (33) (2021): 2101616.
[25] B. Tang, D. Hu, X. Zhao, X. Wang, Z. Liu, Recent developments in chemical vapor deposition of 2D magnetic transition metal chalcogenides, ACS Appl. Electron. Mater. 4 (7) (2022) 3303.
[26] Y. Guo, Y. Cheng, Q. Li, K. Chu, $FeTe_2$ as an earth-abundant metal telluride catalyst for electrocatalytic nitrogen fixation, J. Energy Chem. 56 (2021) 259.
[27] S. Chen, H. Liu, F. Chen, K. Zhou, Y. Xue, Synthesis, transfer, and properties of layered $FeTe_2$ nanocrystals, ACS Nano 14 (9) (2020): 11473.
[28] L. Liu, S. Chen, Z. Lin, X. Zhang, A symmetry-breaking phase in two-dimensional $FeTe_2$ with ferromagnetism above room temperature, J. Phys. Chem. Lett. 11 (18) (2020) 7893.
[29] A. Rahman, D. Zhang, M.U. Rehman, et al., Multiple magnetic phase transitions, electrical and optical properties of $FeTe_2$ single crystals, J. Phys. Condens. Matter 32 (3) (2020): 035808.
[30] L. Tang, J. Tan, H. Nong, B. Liu, H. Cheng, Chemical vapor deposition growth of two-dimensional compound materials: controllability, material quality, and growth mechanism, Acc. Mater. Res. 2 (1) (2020) 36.
[31] Y.Q. Zhao, Q. Liu, B.J. Zhou, G. Yang, S.L. Jiang, Two-dimensional metallic $CoTe_2$ flakes for electrocatalytic hydrogen evolution, Rare Met. 43 (11) (2024) 5860.
[32] H. Jiang, L. Zheng, Z. Liu, X. Wang, Two-dimensional materials: from mechanical properties to flexible mechanical sensors, InfoMat 2 (6) (2019) 1077.
[33] A. CastellanosGomez, V. Singh, H.S.J. van der Zant, G.A. Steele, Mechanics of freely-suspended ultrathin layered materials, Ann. Phys. 527 (1–2) (2014) 27.

[34] G. Cao, H. Gao, Mechanical properties characterization of two-dimensional materials via nanoindentation experiments, Prog. Mater. Sci. 103 (2019) 558.
[35] Q. Zhang, Z. Chang, G. Xu, et al., Strain relaxation of monolayer WS_2 on plastic substrate, Adv. Funct. Mater. 26 (47) (2016) 8707.
[36] L. Yang, X. Cui, J. Zhang, et al., Lattice strain effects on the optical properties of MoS_2 nanosheets, Sci. Rep. 4 (2014) 5649.
[37] P. Li, Z. You, T. Cui, Molybdenum disulfide DC contact MEMS shunt switch, J. Micromech. Microeng. 23 (4) (2013): 045026.
[38] S. Wu, J. Gu, R. Li, et al., Progress on mechanical and tribological characterization of 2D materials by AFM force spectroscopy, Friction 12 (12) (2024) 2627.
[39] T. Cui, S. Mukherjee, P.M. Sudeep, et al., Fatigue of graphene, Nat. Mater. 19 (4) (2020) 405.
[40] S. Jin, Y. Liu, Z. Deng, et al., Strain Gradient Induced Skyrmion in a van der Waals Magnet by Wrinkling, Adv. Mater. 37 (29) (2025): e2501935.
[41] Z.K. Zhu, Z.Y. Li, Z. Qin, et al., Pressure-driven metallization with significant changes of structural and photoelectric properties in two-dimensional $EuSbTe_3$, Rare Met. 43 (11) (2024) 5943.
[42] W. Han, T. Zhang, P. Zhao, et al., Anomalous raman response in 2D magnetic FeTe under uniaxial strain: tetragonal and hexagonal polymorphs, Small 20 (49) (2024): 2400987.
[43] H.D. Lutz, J. Himmrich, B. Müller, G. Schneider, Lattice vibration spectra. LXIX. Lattice dynamics and bonding of pyrite-type chalcogenides and pnictides, Phys. Chem. Miner. 18 (1991) 265.
[44] Y. Yu, M. Cheng, Z. Tao, et al., Phase-Modulated elastic properties of 2D magnetic FeTe: hexagonal and tetragonal polymorphs, Small 20 (18) (2023): 2308357.
[45] A. CastellanosGomez, M. Poot, G.A. Steele, H.S. van der Zant, N. Agrait, G. RubioBollinger, Elastic properties of freely suspended MoS_2 nanosheets, Adv. Mater. 24 (6) (2012) 772.
[46] S. Chandra, A.K.M.A. Islam, Elastic properties of Mono- and poly-crystalline PbO-Type $FeSe_{1-x}Te_x$ (x=0-1.0): a first-principles study, Phys. C Supercond. 470 (22) (2010) 2072.
[47] J. Wang, Y. Li, Z. Zhan, T. Li, L. Zhen, C. Xu, Elastic properties of suspended black phosphorus nanosheets, Appl. Phys. Lett. 108 (1) (2016): 013104.
[48] Q. Wei, X. Peng, Superior mechanical flexibility of phosphorene and few-layer Black phosphorus, Appl. Phys. Lett. 104 (25) (2014): 251915.
[49] H. Lu, X. Liu, J.D. Burton, et al., Enhancement of ferroelectric polarization stability by interface engineering, Adv. Mater. 24 (9) (2012) 1209.
[50] M. Wu, J. Li, Sliding Ferroelectricity in 2D van der Waals Materials: related Physics and Future Opportunities, Proc. Natl. Acad. Sci. USA. 118 (50) (2021): e2115703118.
[51] T.K. Pratt, R. Williams, Non-linear analysis of stick/slip motion, J. Sound Vib. 74 (1981) 531.
[52] C. Gao, D. KuhlmannWilsdorf, D.D. Makel, The dynamic analysis of stick-slip motion, Wear 175 (1994) 1.
[53] Y. Zhao, H.B. Yu, C.Y. Zhao, et al., Anisotropy and synaptic plasticity in CrSBr/WSe_2 heterojunction for advanced neural network applications, Rare Met. 44 (9) (2025) 6483.
[54] L. Feng, Y. Liu, Y. Wang, H. Zhou, Z. Lu, T. Li, Ultra-Compact dual-channel integrated CO_2 infrared gas sensor, Microsyst. Nanoeng. 10 (1) (2024) 151.
[55] P.E. Blöchl, Projector augmented-wave method, Phys. Rev. B 50 (24) (1994): 17953.
[56] G. Kresse, J. Hafner, Ab initio molecular dynamics for open-shell transition metals, Phys. Rev. B 48 (17) (1993): 13115.
[57] G. Kresse, J. Furthmüller, Efficient iterative schemes for ab initio total-energy calculations using a plane-wave basis set, Phys. Rev. B 54 (16) (1996): 11169.
[58] J.P. Perdew, K. Burke, M. Ernzerhof, Generalized gradient approximation made simple, Phys. Rev. Lett. 77 (18) (1996) 3865.
[59] S. Grimme, J. Antony, S. Ehrlich, H. Krieg, A consistent and accurate ab initio parametrization of density functional dispersion correction (DFT-D) for the 94 elements H-Pu, J. Chem. Phys. 132 (15) (2010).
[60] L. Zhang, J. Han, H. Wang, R. Car, W. E, Deep potential molecular dynamics: a scalable model with the accuracy of quantum mechanics, Phys. Rev. Lett. 120 (14) (2018): 143001.
[61] H. Wang, L. Zhang, J. Han, W. E, DeePMD-kit: a deep learning package for many-body potential energy representation and molecular dynamics, Comput. Phys. Commun. 228 (2018) 178.
[62] A.P. Thompson, H.M. Aktulga, R. Berger, et al., LAMMPS - a flexible simulation tool for particle-based materials modeling at the atomic, meso, and continuum scales, Comput. Phys. Commun. 271 (2022): 108171.